Supplemental Material for

Seismica

An unexplained tsunami: Was there megathrust slip during the 2020 M7.6 Sand Point, Alaska, earthquake?

Sean R. Santellanes[1*], Dara E. Goldberg[2], Pablo Koch[3], Diego Melgar[1], William L. Yeck[2], Brendan W. Crowell[4], Jiun-Ting Lin[5]

[1]University of Oregon, Department of Earth Sciences, Eugene, OR, USA

[2]U.S. Geological Survey, National Earthquakes Information Center, Golden, CO, USA

[3]Centro Sismológico Nacional de Chile, Santiago, Chile

[4]University of Washington, Department of Earth and Space Sciences, Seattle, WA, USA

[5]Lawrence Livermore National Laboratory, Livermore, CA, USA

Corresponding author: ssantel2@uoregon.edu

Introduction

This supplement contains Text S1, Figures S1-S24, and table S1 pertaining to additional model analyses.

Text S1: Results of kinematic models K1 and K2

Model K1 allows subfaults to slip with rise times up to 30 s. The resulting model places slip equivalent to moment magnitude (M_w) 7.5 on the megathrust and M_w7.6 on the strike-slip segment (Figure S11). The summation of the two contributions results in a Kagan angle of 13.03º compared to the U.S. Geological Survey (USGS) National Earthquake Information Center (NEIC) W-phase centroid moment tensor (WCMT) (Figure 7).

Synthetic P waves do not fit the first arrival, observed maximum amplitude, or waveform shape (Figure S12). The synthetic Love waves fit the shape and timing of the waveform packets well (Figures S13). Notably, the synthetic Rayleigh waves have modest time lags in nearly all stations (Figure S14). SH body waves fit the observed waveforms poorly, which is expected given their lower weights in the inversion (Figure S15). High-rate Global Navigation Satellite Systems (GNSS) waves have modest fits in the east (E)-component for the first arrival— they largely fail to capture the waveform complexity. The north (N)-components have modest fits between 287º and 52º azimuth. However, the vertical (Z)-component is poorly fit (Figure S16). Strong motion station AK.CHN's (of the Alaska Geophysical Network) E-component can be captured by the model; however, its other components are not. Station AK.S15K is fairly well fit in its N-component, yet, as with AK.CHN, is poorly fit in its other components (Figure S17). Model K1 fits the observations at Deep Ocean Assessment and Reporting of Tsunamis (DART) stations 46409 and 46414 poorly (Figure S11e). These synthetic waveforms appear as solitary Gaussian lumps rather than the complex waveforms in the observed data. The modeled waveform at DART station 46402 arrives 4 minutes early with an underestimated amplitude. The Sand Point coastal sea level station fit is poor; the synthetic tsunami signal arrives 28 minutes early and with poor fit to the first arrival amplitude; however, later arrivals are more consistent with the observations. The modeled tsunami waveform at the King Cove, Alaska, water level station remains poorly fit, severely underpredicting the observed sea level. The fits for the coastal sea level stations in Hawaii are fair yet underestimate the amplitude (Figure S11e).

Of note, model K1 prefers 30-s rise times, the limit of allowable slip duration, indicating that "standard" rise times are insufficient to capture the kinematic source characteristics of the megathrust rupture. Indeed, tsunamigenic earthquakes have been associated with longer than average local slip durations. Thus, we allow longer rise times for the megathrust segment in subsequent models.

Model K2 permits rise times of 0–60 s (Table 1 in main article). Synthetic P waves consistently underpredict the amplitude and fail recreate the observed waveform shape (Figure S18). The modeled Love and Rayleigh surface waves are higher in amplitude than the observed waveforms and have timing issues at most stations (Figures S19 and S20). SH body waves fit the observed waveforms poorly, which is expected given their lower weights (Figure S21). Like K1, the high-rate GNSS waveforms have modest fits for the first arrival in the E-component and fail to capture the full waveform complexity. The N-component is poorly fit outside of azimuths between 287º and 52º. The model poorly fits in the Z-component at all azimuths (Figure S22). The strong motion synthetic fits to the observed data are moderate for station AK.CHN, yet they fail to fit the waveforms for station AK.S15K (Figure S23). Model K2 fits the observations well at DART stations 46409 and 46414 (Figure S18e). However, the solitary Gaussian lump at DART station 46402 arrives 3.5 minutes early with an underestimated amplitude. The Sand Point coastal sea level station synthetic waveform arrives 28 minutes early and with poor fit to the first arrival amplitude; however, later arrivals are more consistent with the observations. The synthetics at the King Cove, Alaska, site severely underpredict the observed sea level. The Hawaii coastal sea level fits underestimate the first arrival amplitude (Figure S18e). The summation of the resulting strike-slip and megathrust rupture results in a Kagan angle of 18.85º (Figure 7). However, the model still prefers the maximum allowable rise times (60 s), indicating that the data would be better fit if even longer rise times were allowed (Figure S18). Again, we increase the limit of allowable rise times for the megathrust in the subsequent model, K3 (see main article).

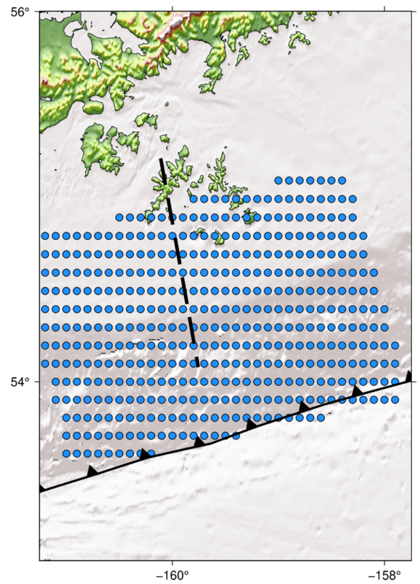

Figure S1. Distribution of Gaussian tsunami sources used in inversion H0. We prescribe Gaussian-shaped sea surface deformation unit source areas in a two-dimensional grid with 10-km spacing across the region of interest, with 428 sources in total. These unit sources have an amplitude of 1 m and a width of 5 km. The Gaussian nature of the tsunami source elements ensures that they overlap at the margins, such that smooth variations of sea surface displacements can be expressed with a sum of these discrete sources. Those sources located on land do not contribute. The dashed black line is the surface projection of the strike-slip geometry. The subduction zone boundary is shown for reference. This map was constructed using GMT 6 (Wessel et al., 2019).

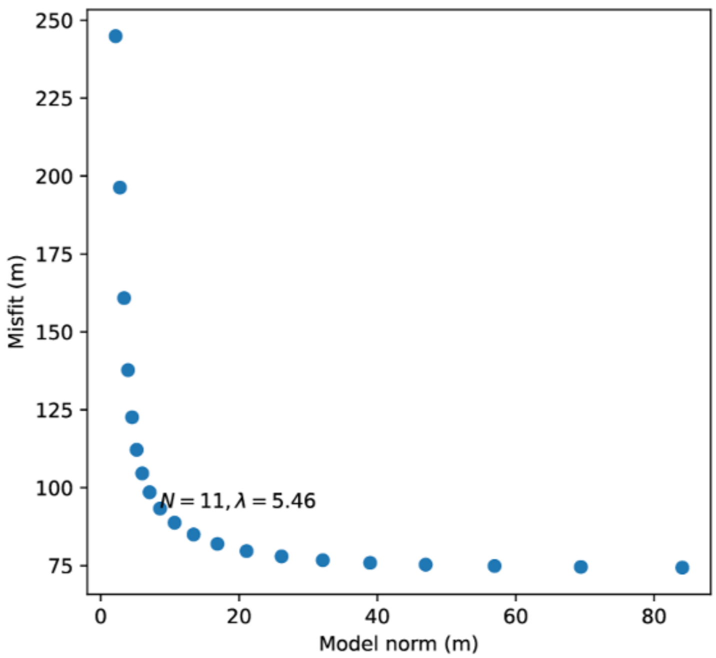

Figure S2. L-curve for the water-level inversion, H0. N is the inversion number. λ is the smoothing parameter. The selected inversion (N=11) is located at the knee of the L-curve.

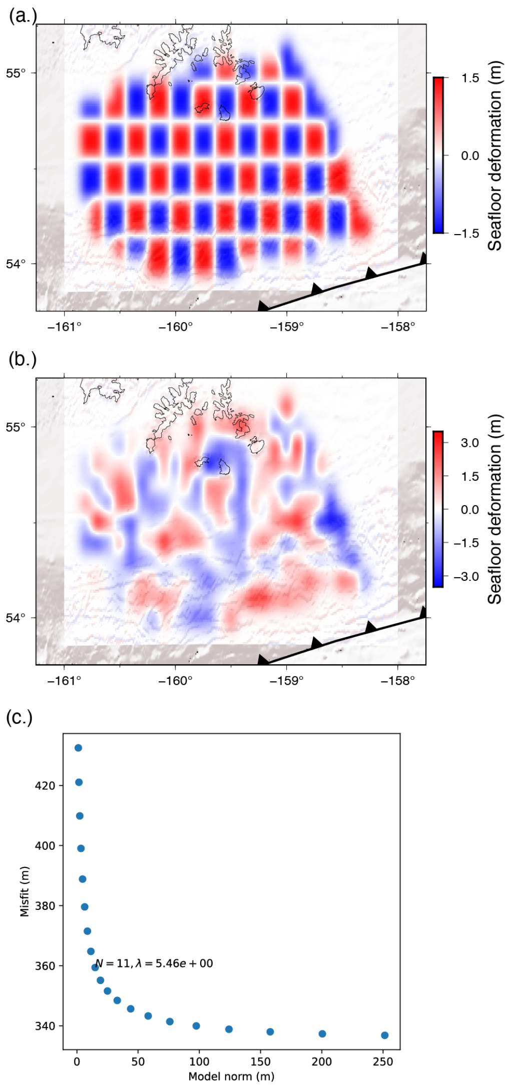

Figure S3. Checkerboard tests for the water-level (hydrodynamic) inversion, H0. (a.) Map view of the input checkerboard, where each checker space is 20-km by 20-km. (b.) Inversion output for selected smoothing parameter. (c.) L-curve to determine the proper smoothing parameter for the checkerboard test. N is the inversion number. λ is the smoothing parameter. Maps in (a.) and (b.) were constructed using GMT 6 (Wessel et al., 2019).

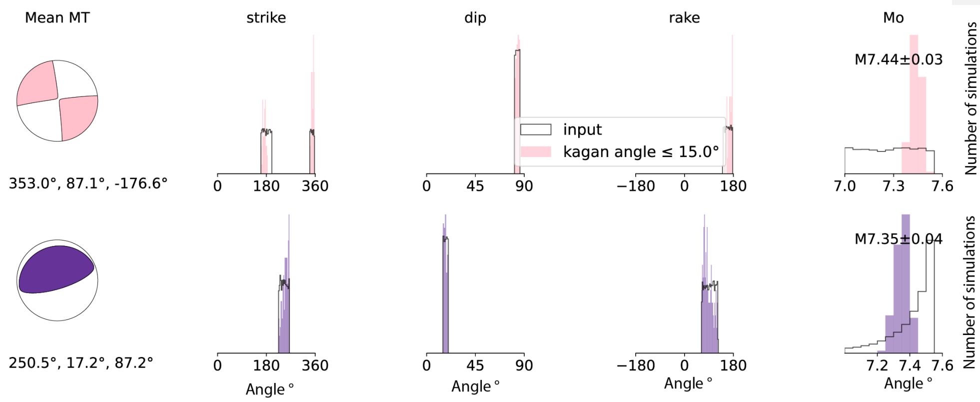

Figure S4. Results from Monte Carlo approach to determine two moment tensors whose combination can reproduce the observed W-phase moment tensor (M_{ww}), given the additional geometric constraint of slip on the megathrust.

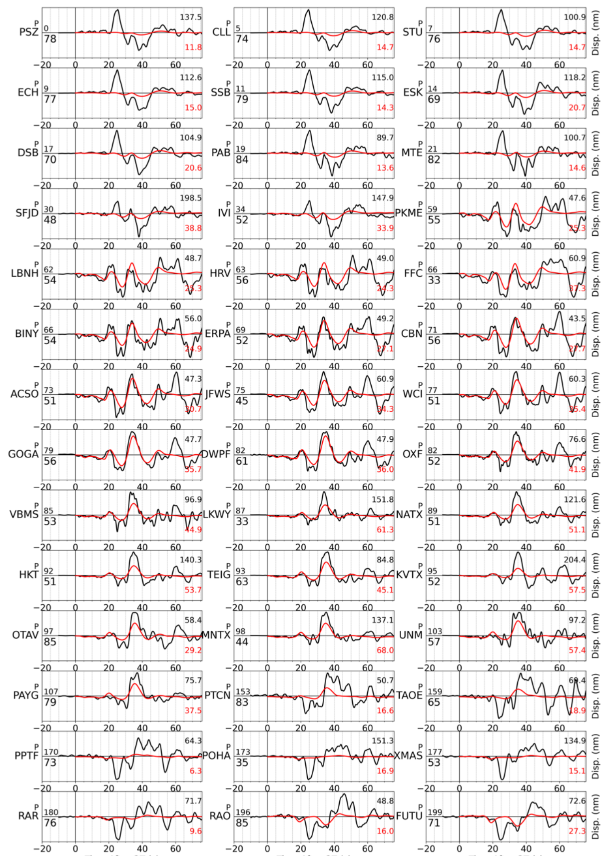

Figure S5. Teleseismic P body wave fits for kinematic inversion K3, with “very long” rise times (0–120 s) along the megathrust and “standard” rise times (0–30 s) along the strike-slip segment. Teleseismic arrival (P) and station code are given to the left of each subplot. The values on the lefthand side of each subplot provide the source-station azimuth (top) and the source-station distance in degrees (bottom). Values on the righthand side of each subplot denote the maximum amplitude of the observed waveform (black) and synthetic waveform (red). Waveforms are given in displacement (nm). See Table S1 for station details.

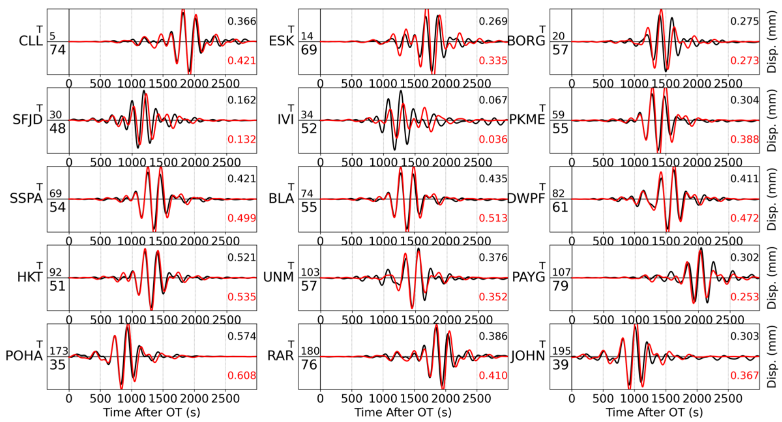

Figure S6. Teleseismic Love surface wave fits for kinematic inversion K3, with "very long" rise times (0–120 s) along the megathrust and "standard" rise times (0–30 s) along the strike-slip segment. Teleseismic arrival (T) and station code are given to the left of each subplot. The values on the lefthand side of each subplot provide the source-station azimuth (top), and the source-station distance in degrees (bottom). Values on the righthand side of each subplot denote the maximum amplitude of the observed waveform (black) and synthetic waveform (red). Waveforms are given in displacement (mm). See Table S1 for station details.

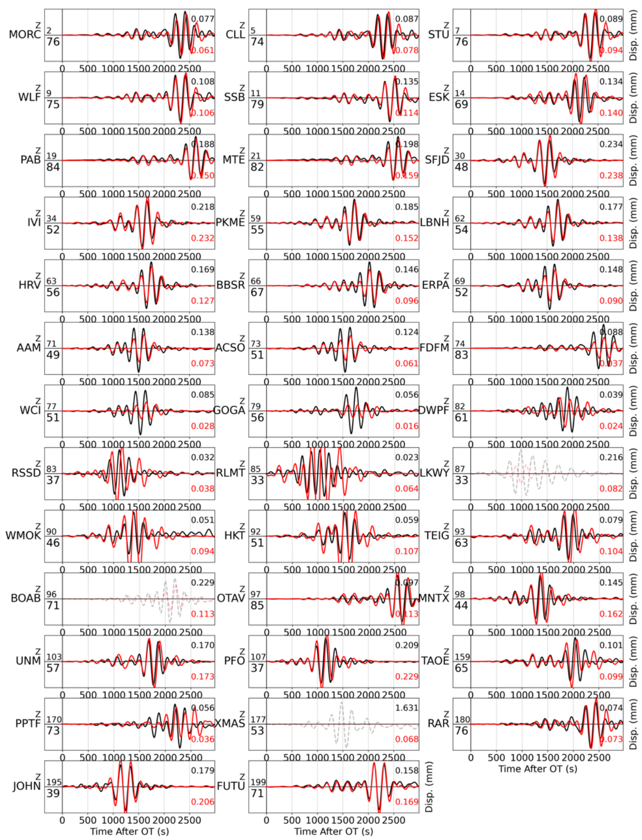

Figure S7. Teleseismic Rayleigh surface wave fits for kinematic inversion K3, with “very long” rise times (0–120 s) along the megathrust and “standard” rise times (0–30 s) along the strike-slip segment. Teleseismic arrival (Z) and station code are given to the left of each subplot. The values on the lefthand side of each subplot provide the source-station azimuth (top) and the source-station distance in degrees (bottom). Values on the righthand side of each subplot denote the maximum amplitude of the observed waveform (black) and synthetic waveform (red). Waveforms shown as a dashed black line received zero weight in the inversion due to poor fits. Waveforms are given in displacement (mm). See Table S1 for station details.

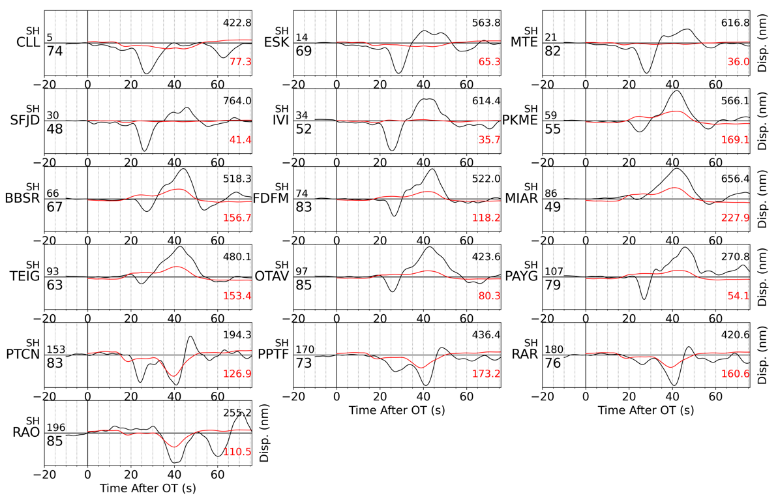

Figure S8. Teleseismic SH body wave fits for kinematic inversion K3, with "very long" rise times (0–120 s) along the megathrust and "standard" rise times (0–30 s) along the strike-slip segment. Teleseismic arrival (SH) and station code are given to the left of each subplot. The values on the lefthand side of each subplot provide the source-station azimuth (top) and the source-station distance in degrees (bottom). Values on the righthand side of each subplot denote the maximum amplitude of the observed waveform (black) and synthetic waveform (red). Waveforms are given in displacement (nm). See Table S1 for station details.

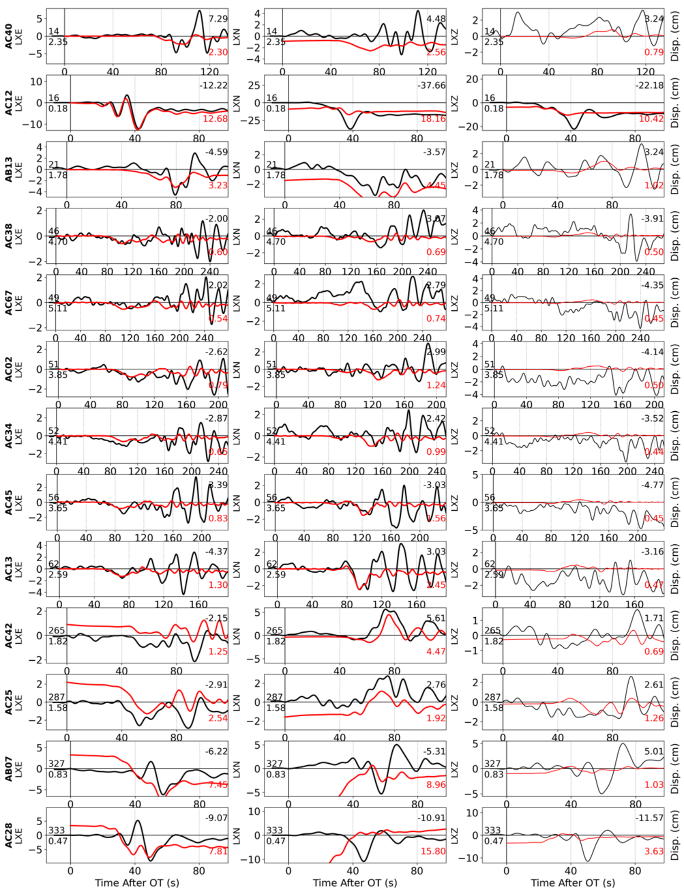

Figure S9. High rate GNSS waveform fits for LXE (left), LXN (center), and LXZ (right) components of displacement used in kinematic inversion K3. Station codes are given to the left of the waveforms. The values on the lefthand side of each subplot provide the source-station azimuth (top) and the source-station distance in degrees (bottom). Values on the righthand side of each subplot denote the maximum amplitude of the observed waveform (black) and synthetic waveform (red). Line thickness is proportional to weight, with the Z-component receiving one-half the weight of the horizontal components. Waveforms are given in displacement (cm). See Table S1 for station details.

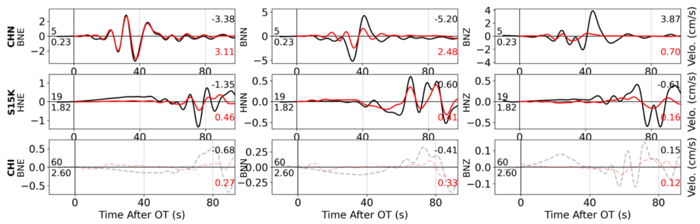

Figure S10. Strong motion waveform fits for components BNE/HNE (left), BNN/HNN (center), and BNZ/HNZ (right) used in kinematic inversion K3. Alaska Geophysical Network station codes are given to the left of the waveforms. The values on the lefthand side of each subplot provide the source-station azimuth (top) and the source-station distance in degrees (bottom). Values on the righthand side of each subplot denote the maximum amplitude of the observed waveform (black) and synthetic waveform (red). Station CHI is shown as a dashed line because it received zero weight in the inversion due to poor fits. Waveforms are given in velocity (cm/s). See Table S1 for station details.

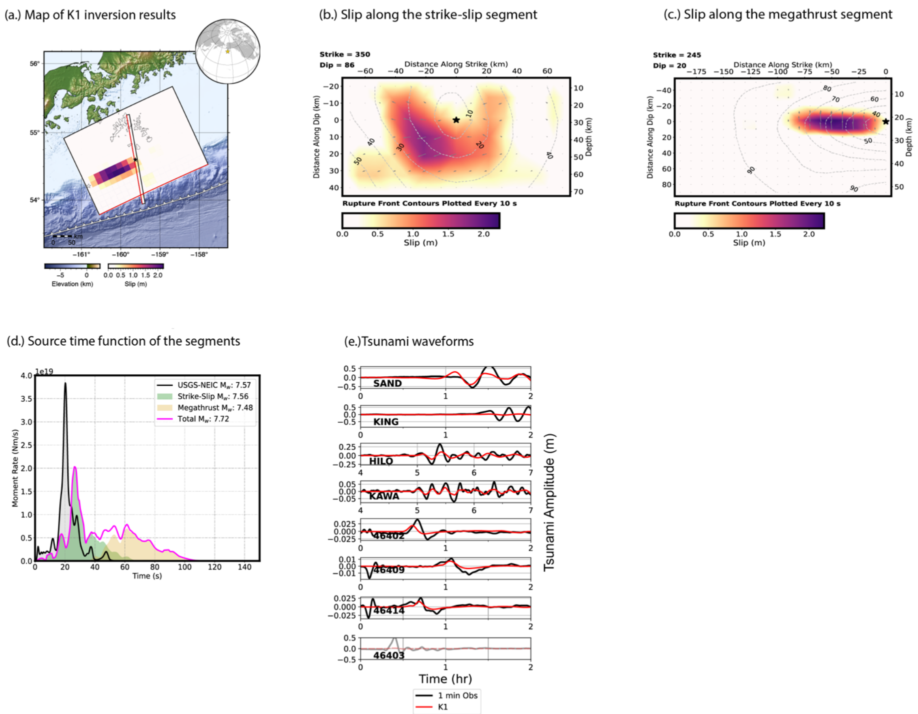

Figure S11. Model K1 results — “standard” allowed rise times of 0–30 s. (a.) Map showing the geographical distribution of slip along the megathrust as well as the strike-slip geometry. Black star shows the event hypocenter, and white star shows the nucleation point for the megathrust slip. Red lines indicate the up-dip edge of the two fault orientations. This map was constructed using GMT 6 (Wessel et al., 2019).

(b.) Smoothed slip distribution and rupture time contours for the strike-slip segment. Small gray arrows indicate rake direction, scaled by amplitude of slip (c.) Same as (b.) but for the megathrust segment. Note that the rupture time contours start 29.5 s later, denoting the delayed slip to nucleation point N3 (star). (d.) Moment rate functions for U.S. Geological Survey National Earthquake Information Center (USGS-NEIC) solution (black) and this study (pink) with contribution from the strike-slip segment (green) and megathrust (yellow) (e.) Observed (black) and synthetic (red) tsunami waveforms. See Table S1 for station details.

Commented [GE1]: Remove title above fig (or add one to fig S6) for consistency

Commented [SS2R1]: Removed title from this figure to make it consistent.

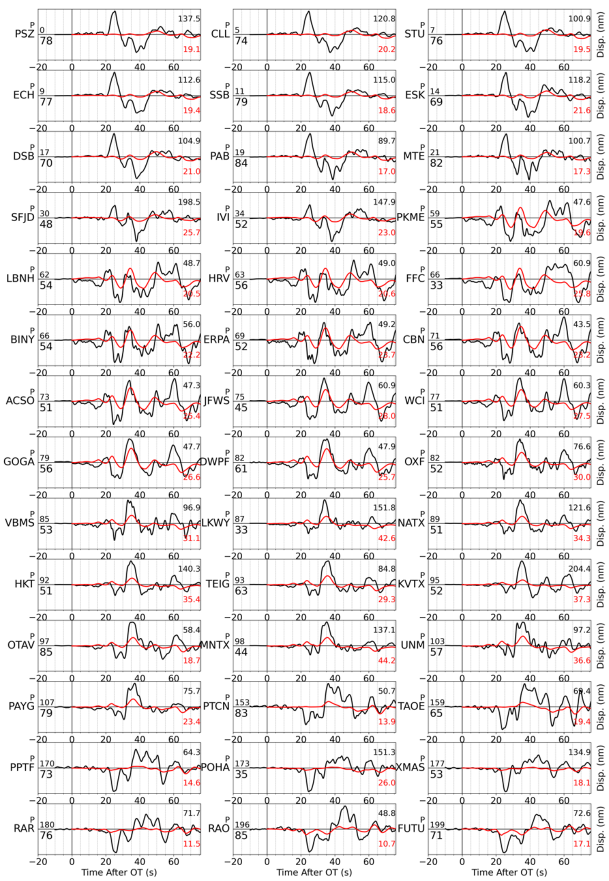

Figure S12. Teleseismic P body wave fits for kinematic inversion K1, with "standard" rise times along both the megathrust and strike-slip segments. Teleseismic arrival (P) and station code are given to the left of each subplot. The values on the lefthand side of each subplot provide the source-station azimuth (top) and the source-station distance in degrees (bottom). Values on the righthand side of each subplot denote the maximum amplitude of the observed waveform (black) and synthetic waveform (red). Waveforms are given in displacement (nm). See Table S1 for station details.

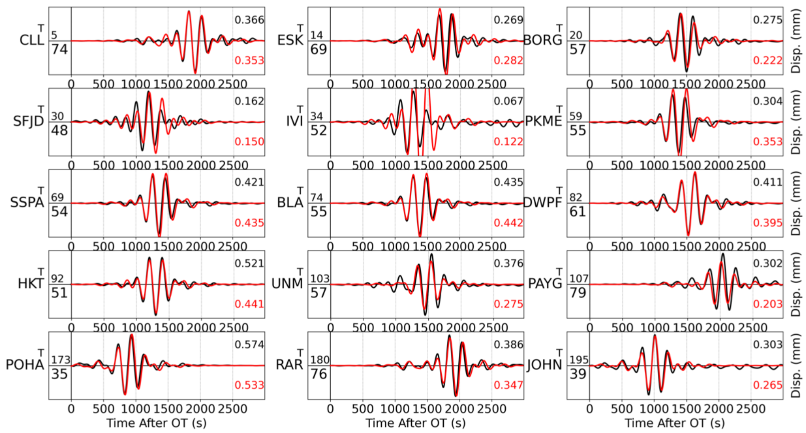

Figure S13. Teleseismic Love surface wave fits for kinematic inversion K1, with "standard" rise times. Teleseismic arrival (T) and station code are given to the left of each subplot. The values on the lefthand side of each subplot provide the source-station azimuth (top) and the source-station distance in degrees (bottom). Values on the righthand side of each subplot denote the maximum amplitude of the observed waveform (black) and synthetic waveform (red). Waveforms are given in displacement (mm). See Table S1 for station details.

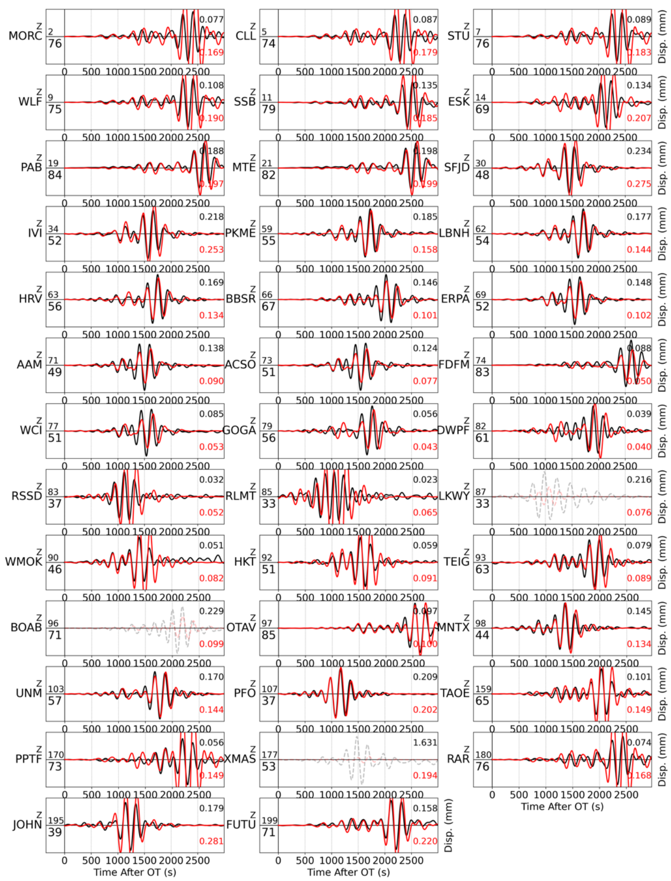

Figure S14. Teleseismic Rayleigh surface wave fits for kinematic inversion K1, with "standard" rise times. Teleseismic arrival (Z) and station code are given to the left of each subplot. The values on the lefthand side of each subplot provide the source-station azimuth (top) and the source-station distance in degrees (bottom). Values on the righthand side of each subplot denote the maximum amplitude of the observed waveform (black) and synthetic waveform (red). Waveforms shown as a dashed black line received zero weight in the inversion due to poor fits. Waveforms are given in displacement (mm). See Table S1 for station details.

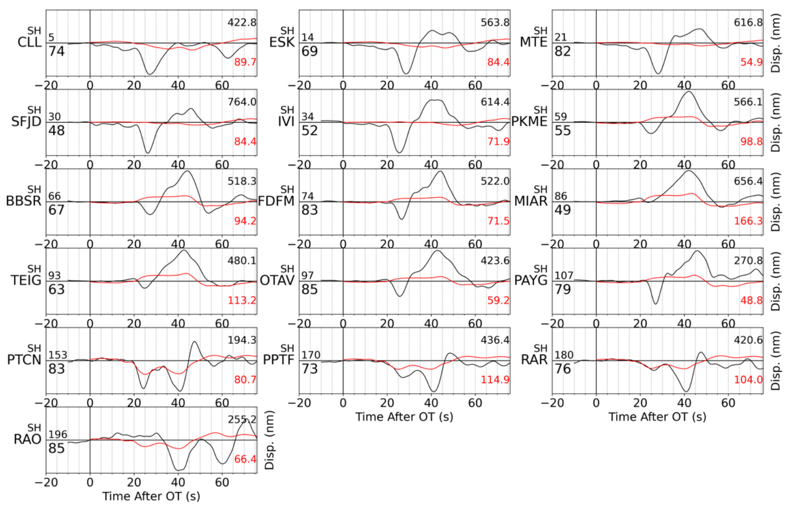

Figure S15. Teleseismic SH body wave fits for kinematic inversion K1, with "standard" rise times along both the megathrust and strike-slip segments. Teleseismic arrival (SH) and station code are given to the left of each subplot. The values on the lefthand side of each subplot provide the source-station azimuth (top) and the source-station distance in degrees (bottom). Values on the righthand side of each subplot denote the maximum amplitude of the observed waveform (black) and synthetic waveform (red). Waveforms are given in displacement (nm). See Table S1 for station details.

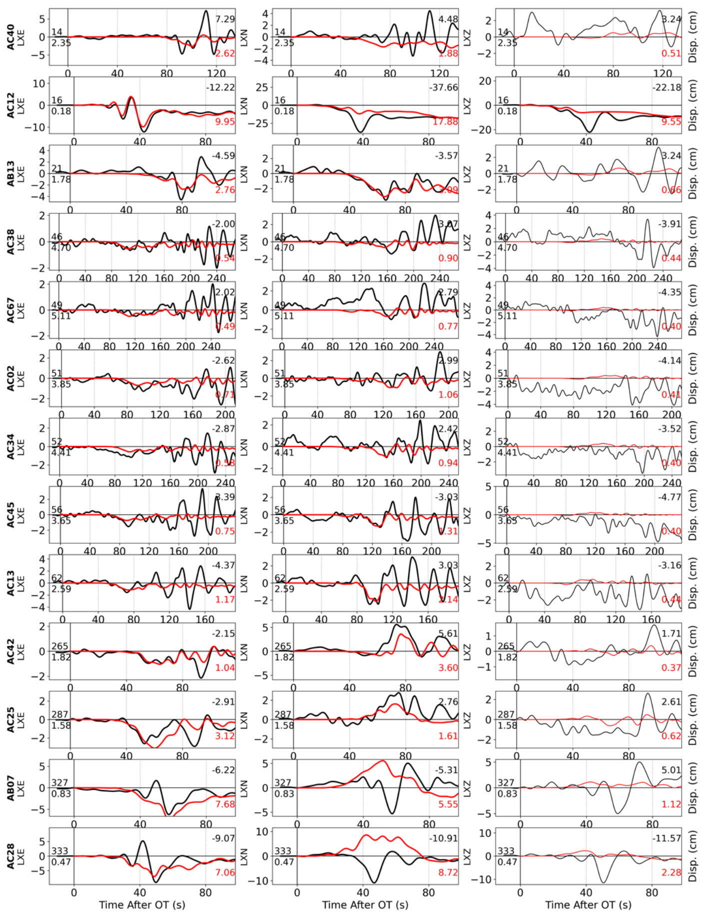

Figure S16. High-rate Global Navigation Satellite System (GNSS) waveform fits for stations LXE (left), LXN (center), and LXZ (right) components of displacement used in kinematic inversion K1. Station codes are given to the left of the waveforms. The values on the lefthand side of each subplot provide the source-station azimuth (top) and the source-station distance in degrees (bottom). Values on the righthand side of each subplot denote the maximum amplitude of the observed waveform (black) and synthetic waveform (red). Line thickness is proportional to weight, with the Z-component receiving half the weight of the horizontal components. Waveforms are given in displacement (cm). See Table S1 for station details.

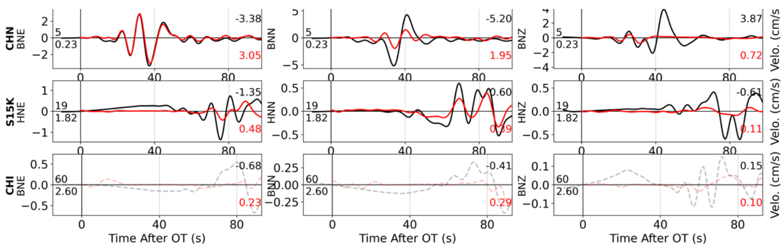

Figure S17. Strong motion waveform fits for components BNE/HNE (left), BNN/HNN (center), and BNZ/HNZ (right) used in kinematic inversion K1. Station codes are given to the left of the waveforms. The values on the lefthand side of each subplot provide the source-station azimuth (top) and the source-station distance in degrees (bottom). Values on the righthand side of each subplot denote the maximum amplitude of the observed waveform (black) and synthetic waveform (red). Station CHI is shown as a dashed line because it received zero weight in the inversion due to poor fits. Waveforms are given in velocity (cm/s). See Table S1 for station details.

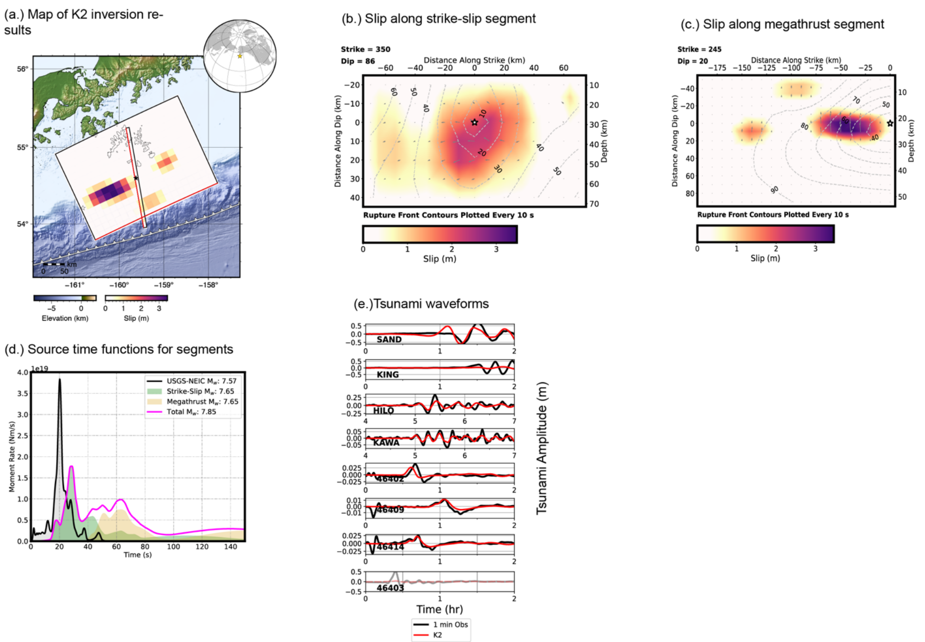

Figure S18. Model K2 results — "long" allowed rise times of 0-60 s (a.) Map showing the geographical distribution of slip along the megathrust as well as the strike-slip geometry. Black star shows the event hypocenter, and white star shows the nucleation point for the megathrust. Red lines indicate the up-dip edge of the two fault orientations. This map was constructed using GMT 6 (Wessel et al., 2019). (b.) Smoothed slip distribution and rupture time contours for the strike-slip segment. Small gray arrows indicate rake direction, scaled by amplitude of slip (c.) Same as (b.) but for the megathrust segment. Note that the rupture time contours start 29.5 s later, denoting the delayed slip to nucleation point N3 (star). (d.) Moment rate functions for U.S. Geological Survey National Earthquake Information Center (USGS-NEIC) (black) and this study (pink) with contribution from the strike-slip segment (green) and megathrust (yellow) (e.) Observed (black) and synthetic (red) tsunami waveforms. See Table S1 for station details.

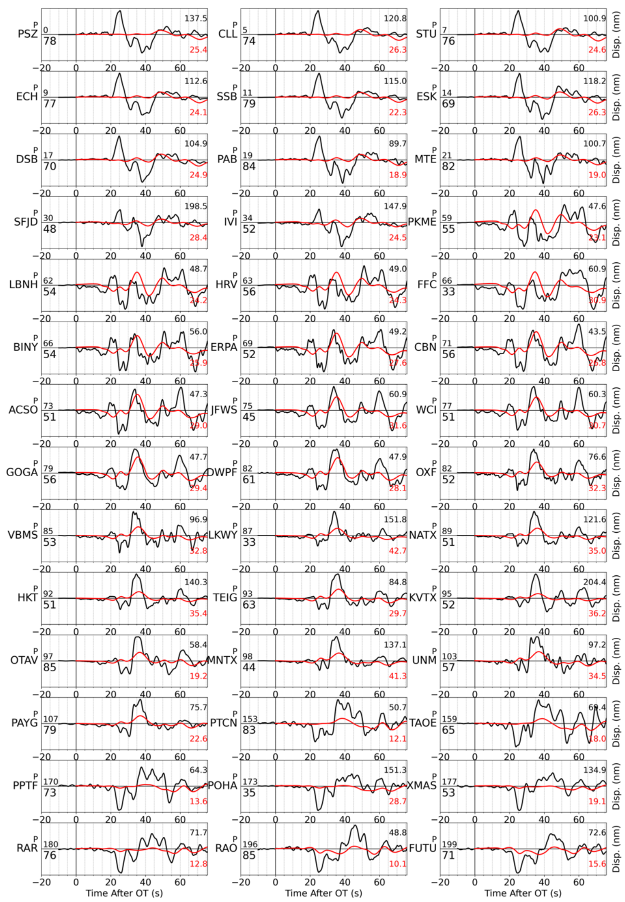

Figure S19. Teleseismic P body wave fits for kinematic inversion K2, with "long" rise times along both the megathrust and strike-slip segments. Teleseismic arrival (P) and station code are given to the left of each subplot. The values on the lefthand side of each subplot provide the source-station azimuth (top) and the source-station distance in degrees (bottom). Values on the righthand side of each subplot denote the maximum amplitude of the observed waveform (black) and synthetic waveform (red). Waveforms are given in displacement (nm). See Table S1 for station details.

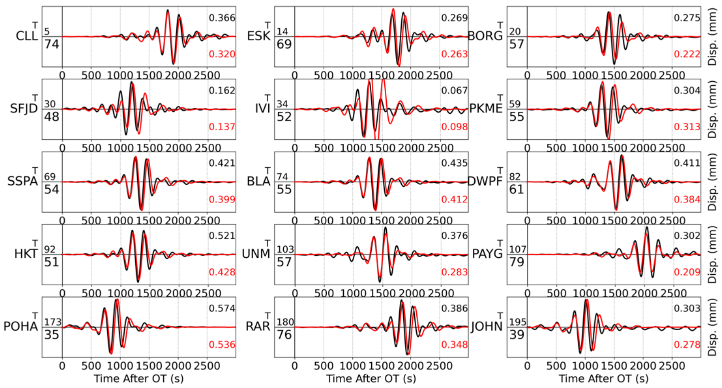

Figure S20. Teleseismic Love surface wave fits for kinematic inversion K2, with “long” rise times. Teleseismic arrival (T) and station code are given to the left of each subplot. The values on the lefthand side of each subplot provide the source-station azimuth (top) and the source-station distance in degrees (bottom). Values on the righthand side of each subplot denote the maximum amplitude of the observed waveform (black) and synthetic waveform (red). Waveforms are given in displacement (mm). See Table S1 for station details.

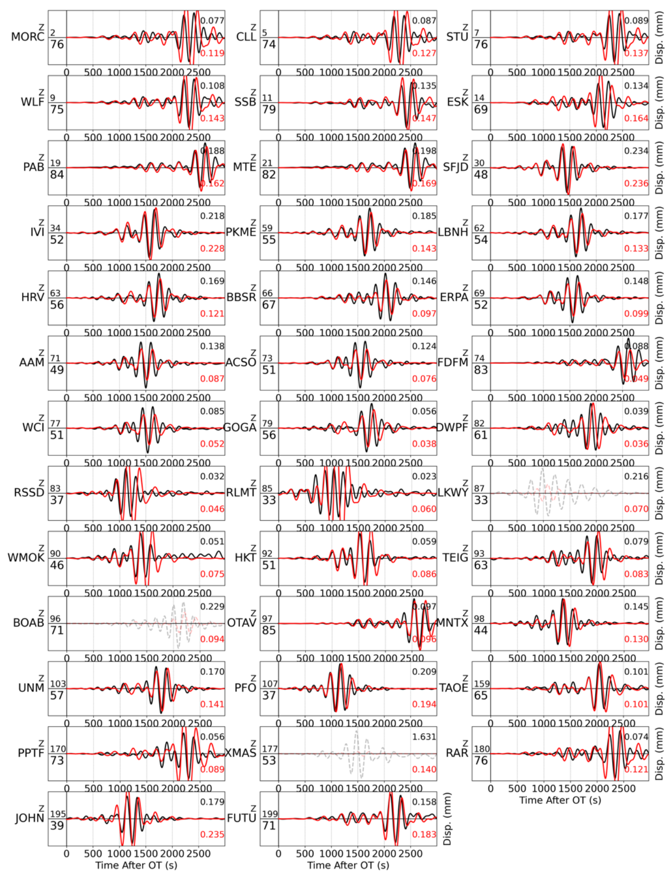

Figure S21. Teleseismic Rayleigh surface wave fits for kinematic inversion K2, with "long" rise times. Teleseismic arrival (Z) and station code are given to the left of each subplot. The values on the lefthand side of each subplot provide the source-station azimuth (top) and the source-station distance in degrees (bottom). Values on the righthand side of each subplot denote the maximum amplitude of the observed waveform (black) and synthetic waveform (red). Waveforms shown as a dashed black line received zero weight in the inversion due to poor fits. Waveforms are given in displacement (mm). See Table S1 for station details.

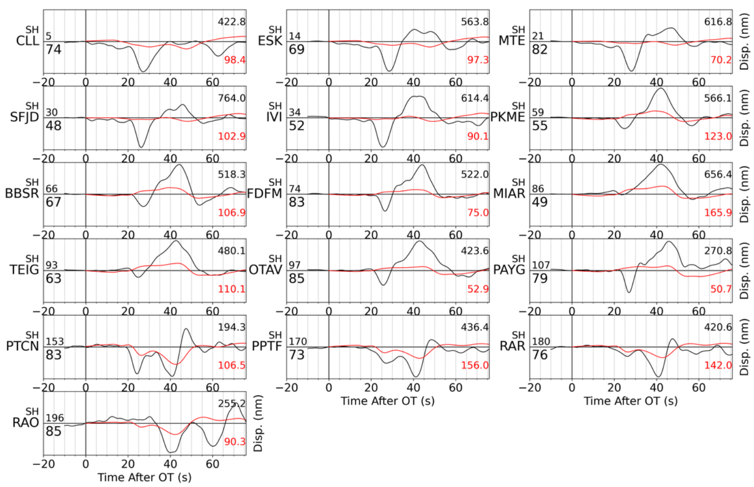

Figure S22. Teleseismic SH body wave fits for kinematic inversion K2, with “long” rise times along both the megathrust and strike-slip segments. Teleseismic arrival (SH) and station code are given to the left of each subplot. The values on the lefthand side of each subplot provide the source-station azimuth (top) and the source-station distance in degrees (bottom). Values on the righthand side of each subplot denote the maximum amplitude of the observed waveform (black) and synthetic waveform (red). Waveforms are given in displacement (nm). See Table S1 for station details.

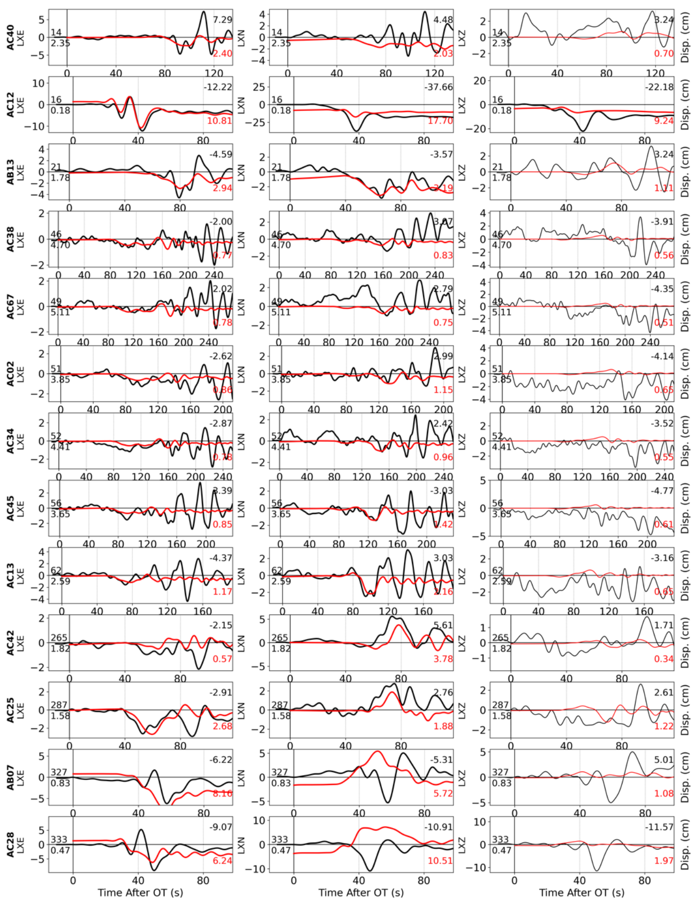

Figure S23. High-rate GNSS waveform fits for LXE (left), LXN (center), and LXZ (right) components of displacement used in kinematic inversion K2. Station codes are given to the left of the waveforms. The values on the lefthand side of each subplot provide the source-station azimuth (top) and the source-station distance in degrees (bottom). Values on the righthand side of each subplot denote the maximum amplitude of the observed waveform (black) and synthetic waveform (red). Line thickness is proportional to weight, with the Z-component receiving half the weight of the horizontal components. Waveforms are given in displacement (cm). See Table S1 for station details.

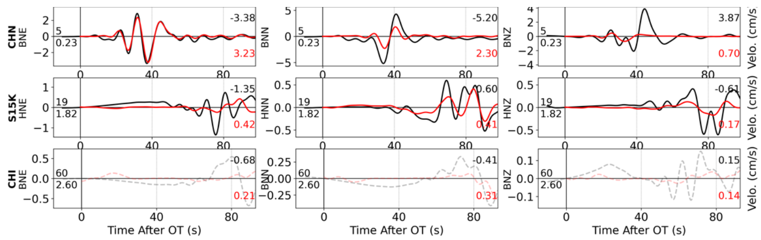

Figure S24. Strong motion waveform fits for BNE/HNE (left), BNN/HNN (center), and BNZ/HNZ (right) components used in kinematic inversion K2. Station codes are given to the left of the waveforms. The values on the lefthand side of each subplot provide the source-station azimuth (top) and the source-station distance in degrees (bottom). Values on the righthand side of each subplot denote the maximum amplitude of the observed waveform (black) and synthetic waveform (red). Station CHI is shown as a dashed line because it received zero weight in the inversion due to poor fits. Waveforms are given in velocity (cm/s). See Table S1 for station details.

Table S1. Locations of observing stations, denoting which stations were used in the various inversions. SGNSS refers to static Global Navigation Satellite System (GNSS), HRGNSS refers to high-rate GNSS, CSLS refers to coastal sea level, and STR refers to strong motion stations. P, SH, Rayleigh, and Love refer to the teleseismic arrivals used. Teleseismic observations are from networks IU (Albuquerque Seismological Laboratory/USGS, 2014), II (Scripps Institution of Oceanography, 1986), US (Albuquerque Seismological Laboratory (ASL)/USGS, 1990), G (Institut de physique du globe de Paris (IPGP) and École et Observatoire des Sciences de la Terre de Strasbourg (EOST), 1982), GR (GEOFON Data Centre, 1993), and GE (Federal Institute for Geosciences and Natural Resources, 1976). Strong motion accelerometer observations are from network AK (Alaska Geophysical Network, University of Alaska Fairbanks, 1987). *This material is based on services provided by the GAGE Facility, operated by UNAVCO, Inc., with support from the National Science Foundation, the National Aeronautics and Space Administration, and the U.S. Geological Survey under NSF Cooperative Agreement EAR-1724794.* Coastal water level data is provided by the Intergovernmental Oceanographic Commission and operated by the National Oceanic and Atmospheric Administration (CO-OPS, 2007). Deep-ocean Assessment and Reporting of Tsunamis (DART) stations are operated by the National Oceanic and Atmospheric Administration (NOAA, 2005). Network codes do not exist for GNSS, DART, or CSLS stations and are denoted by “-”.

NETWORK CODE	**STATION NAME**	**LATITUDE** (°N)	**LONGITUDE** (°E)	**OBSERVATION**	**INVERSIONS INCLUDED**
GE	PSZ	47.918	19.894	P	K1, K2, K3
GR	CLL	51.308	13.002	P	K1, K2, K3
GE	STU	48.772	9.195	P	K1, K2, K3
G	ECH	48.216	7.159	P	K1, K2, K3
G	SSB	45.279	4.542	P	K1, K2, K3
II	ESK	55.317	-3.205	P	K1, K2, K3
GE	DSB	53.245	-6.376	P	K1, K2, K3
IU	PAB	39.545	-4.35	P	K1, K2, K3
GE	MTE	40.4	-7.544	P	K1, K2, K3
IU	SFJD	66.996	-50.621	P	K1, K2, K3
G	IVI	61.206	-48.171	P	K1, K2, K3
US	PKME	45.264	-69.292	P	K1, K2, K3
US	LBNH	44.24	-71.926	P	K1, K2, K3
IU	HRV	42.506	-71.558	P	K1, K2, K3
II	FFC	54.725	-101.978	P	K1, K2, K3
US	BINY	42.199	-75.986	P	K1, K2, K3
US	ERPA	42.118	-79.989	P	K1, K2, K3
US	CBN	38.205	-77.373	P	K1, K2, K3
US	ACSO	40.232	-82.982	P	K1, K2, K3
US	JFWS	42.914	-90.248	P	K1, K2, K3
IU	WCI	38.229	-86.294	P	K1, K2, K3
US	GOGA	33.411	-83.467	P	K1, K2, K3

IU	DWPF	28.11	-81.433	P	K1, K2, K3
US	OXF	34.512	-89.409	P	K1, K2, K3
US	VBMS	32.219	-90.518	P	K1, K2, K3
US	LKWY	44.565	-110.4	P	K1, K2, K3
US	NATX	31.76	-94.661	P	K1, K2, K3
IU	HKT	29.965	-95.838	P	K1, K2, K3
IU	TEIG	20.226	-88.276	P	K1, K2, K3
US	KVTX	27.546	-97.893	P	K1, K2, K3
IU	OTAV	0.238	-78.451	P	K1, K2, K3
US	MNTX	31.698	-105.382	P	K1, K2, K3
G	UNM	19.33	-99.178	P	K1, K2, K3
IU	PAYG	-0.674	-90.286	P	K1, K2, K3
IU	PTCN	-25.071	-130.095	P	K1, K2, K3
G	TAOE	-8.855	-140.148	P	K1, K2, K3
G	PPTF	-17.59	-149.565	P	K1, K2, K3
IU	POHA	19.757	-155.533	P	K1, K2, K3
IU	XMAS	2.045	-157.446	P	K1, K2, K3
IU	RAR	-21.212	-159.773	P	K1, K2, K3
IU	RAO	-29.245	-177.929	P	K1, K2, K3
G	FUTU	-14.308	-178.121	P	K1, K2, K3
GR	CLL	51.308	13.002	SH	K1, K2, K3
II	ESK	55.317	-3.205	SH	K1, K2, K3
GE	MTE	40.4	-7.544	SH	K1, K2, K3
IU	SFJD	66.996	-50.621	SH	K1, K2, K3
G	IVI	61.206	-48.171	SH	K1, K2, K3
US	PKME	45.264	-69.292	SH	K1, K2, K3
IU	BBSR	32.371	-64.696	SH	K1, K2, K3
G	FDFM	14.735	-61.16	SH	K1, K2, K3
US	MIAR	34.545	-93.576	SH	K1, K2, K3
IU	TEIG	20.226	-88.276	SH	K1, K2, K3
IU	OTAV	0.238	-78.451	SH	K1, K2, K3
IU	PAYG	-0.674	-90.286	SH	K1, K2, K3
IU	PTCN	-25.071	-130.095	SH	K1, K2, K3
G	PPTF	-17.59	-149.565	SH	K1, K2, K3
IU	RAR	-21.212	-159.773	SH	K1, K2, K3
IU	RAO	-29.245	-177.929	SH	K1, K2, K3
AK	S15K	56.306	-158.54	STR	K1, K2, K3
AK	CHN	54.831	-159.589	STR	K1, K2, K3
AK	CHI	55.822	-155.622	STR	K1, K2, K3
—	AB07	55.349	-160.477	HRGNSS	K1, K2, K3
—	AB13	56.307	-158.504	HRGNSS	K1, K2, K3
—	AC02	56.951	-154.183	HRGNSS	K1, K2, K3

—	AC12	54.831	-159.59	HRGNSS	K1, K2, K3
—	AC13	55.822	-155.622	HRGNSS	K1, K2, K3
—	AC25	55.089	-162.314	HRGNSS	K1, K2, K3
—	AC28	55.078	-160.049	HRGNSS	K1, K2, K3
—	AC34	57.22	-153.279	HRGNSS	K1, K2, K3
—	AC38	57.754	-153.342	HRGNSS	K1, K2, K3
—	AC40	56.93	-158.619	HRGNSS	K1, K2, K3
—	AC42	54.472	-162.784	HRGNSS	K1, K2, K3
—	AC45	56.564	-154.181	HRGNSS	K1, K2, K3
—	AC67	57.791	-152.425	HRGNSS	K1, K2, K3
—	AC25	55.089	-162.314	SGNSS	K1, K2, K3
—	AC67	57.791	-152.425	SGNSS	K1, K2, K3
—	AC45	56.564	-154.181	SGNSS	K1, K2, K3
—	AC34	57.22	-153.279	SGNSS	K1, K2, K3
—	AC12	54.831	-159.59	SGNSS	S1, S2, K1, K2, K3
—	AC40	56.93	-158.619	SGNSS	K1, K2, K3
—	AC13	55.822	-155.622	SGNSS	K1, K2, K3
—	AC42	54.472	-162.784	SGNSS	K1, K2, K3
—	AC28	55.078	-160.049	SGNSS	K1, K2, K3
—	AC02	56.951	-154.183	SGNSS	K1, K2, K3
—	AC38	57.754	-153.342	SGNSS	K1, K2, K3
—	AB13	56.307	-158.504	SGNSS	K1, K2, K3
—	AB07	55.349	-160.477	SGNSS	K1, K2, K3
—	46409	55.318	-148.547	DART	H0, S1, S2, K1, K2, K3
—	46402	50.983	-163.943	DART	H0, S1, S2, K1, K2, K3
—	46414	53.764	-152.416	DART	H0, S1, S2, K1, K2, K3
—	46403	52.663	-156.778	DART	None
—	SAND	55.331	-160.505	CSLS	H0, S1, S2
—	KING	55.060	-162.327	CSLS	H0, S1, S2
—	HILO	19.730	-155.060	CSLS	None
—	KAWA	20.036	-155.830	CSLS	None
GE	MORC	49.777	17.543	Rayleigh	K1, K2, K3
GR	CLL	51.308	13.002	Rayleigh	K1, K2, K3
GE	STU	48.772	9.195	Rayleigh	K1, K2, K3
GE	WLF	49.665	6.153	Rayleigh	K1, K2, K3
G	SSB	45.279	4.542	Rayleigh	K1, K2, K3
II	ESK	55.317	-3.205	Rayleigh	K1, K2, K3
IU	PAB	39.545	-4.35	Rayleigh	K1, K2, K3
GE	MTE	40.4	-7.544	Rayleigh	K1, K2, K3

IU	SFJD	66.996	-50.621	Rayleigh	K1, K2, K3
G	IVI	61.206	-48.171	Rayleigh	K1, K2, K3
US	PKME	45.264	-69.292	Rayleigh	K1, K2, K3
US	LBNH	44.24	-71.926	Rayleigh	K1, K2, K3
IU	HRV	42.506	-71.558	Rayleigh	K1, K2, K3
IU	BBSR	32.371	-64.696	Rayleigh	K1, K2, K3
US	ERPA	42.118	-79.989	Rayleigh	K1, K2, K3
US	AAM	42.301	-83.657	Rayleigh	K1, K2, K3
US	ACSO	40.232	-82.982	Rayleigh	K1, K2, K3
G	FDFM	14.735	-61.16	Rayleigh	K1, K2, K3
IU	WCI	38.229	-86.294	Rayleigh	K1, K2, K3
US	GOGA	33.411	-83.467	Rayleigh	K1, K2, K3
IU	DWPF	28.11	-81.433	Rayleigh	K1, K2, K3
IU	OTAV	0.238	-78.451	Rayleigh	K1, K2, K3
US	MNTX	31.698	-105.382	Rayleigh	K1, K2, K3
G	UNM	19.33	-99.178	Rayleigh	K1, K2, K3
II	PFO	33.611	-116.455	Rayleigh	K1, K2, K3
G	TAOE	-8.855	-140.148	Rayleigh	K1, K2, K3
G	PPTF	-17.59	-149.565	Rayleigh	K1, K2, K3
IU	RAR	-21.212	-159.773	Rayleigh	K1, K2, K3
IU	JOHN	16.733	-169.529	Rayleigh	K1, K2, K3
G	FUTU	-14.308	-178.121	Rayleigh	K1, K2, K3
GR	CLL	51.308	13.002	Love	K1, K2, K3
II	ESK	55.317	-3.205	Love	K1, K2, K3
II	BORG	64.747	-21.327	Love	K1, K2, K3
IU	SFJD	66.996	-50.621	Love	K1, K2, K3
G	IVI	61.206	-48.171	Love	K1, K2, K3
US	PKME	45.264	-69.292	Love	K1, K2, K3
IU	SSPA	40.636	-77.888	Love	K1, K2, K3
US	BLA	37.211	-80.42	Love	K1, K2, K3
IU	DWPF	28.11	-81.433	Love	K1, K2, K3
IU	HKT	29.965	-95.838	Love	K1, K2, K3
G	UNM	19.33	-99.178	Love	K1, K2, K3
IU	PAYG	-0.674	-90.286	Love	K1, K2, K3
IU	POHA	19.757	-155.533	Love	K1, K2, K3
IU	RAR	-21.212	-159.773	Love	K1, K2, K3
IU	JOHN	16.733	-169.529	Love	K1, K2, K3
US	LKWY	44.565	-110.4	Rayleigh	K1, K2, K3
GE	BOAB	12.449	-85.666	Rayleigh	K1, K2, K3
IU	XMAS	2.045	-157.446	Rayleigh	K1, K2, K3
IU	RSSD	44.121	-104.036	Rayleigh	K1, K2, K3
US	RLMT	45.122	-109.267	Rayleigh	K1, K2, K3

IU	TEIG	20.226	-88.276	Rayleigh	K1, K2, K3
US	WMOK	34.738	-98.781	Rayleigh	K1, K2, K3
IU	HKT	29.965	-95.838	Rayleigh	K1, K2, K3

References

Alaska Earthquake Center, University of Alaska Fairbanks. (1987). *Alaska Geophysical Network* [Data set]. International Federation of Digital Seismograph Networks. https://doi.org/10.7914/SN/AK

Albuquerque Seismological Laboratory (ASL)/USGS. (1990). *United States National Seismic Network* [Data set]. International Federation of Digital Seismograph Networks. https://doi.org/10.7914/SN/US

Albuquerque Seismological Laboratory/USGS. (2014). *Global Seismograph Network (GSN - IRIS/USGS)* [Data set]. International Federation of Digital Seismograph Networks. https://doi.org/10.7914/SN/IU

Center for Operational Oceanographic Products and Services (CO-OPS) (2007): CO-OPS 1-minute Tsunami Water Level Data. NOAA National Centers for Environmental Information. https://doi.org/10.7289/V59884XF

Federal Institute for Geosciences and Natural Resources. (1976). *German Regional Seismic Network (GRSN)*. Bundesanstalt für Geowissenschaften und Rohstoffe. https://doi.org/10.25928/mbx6-hr74

GEOFON Data Centre. (1993). *GEOFON Seismic Network* [Data set]. GFZ Data Services. https://doi.org/10.14470/TR560404

Institut de physique du globe de Paris (IPGP), & École et Observatoire des Sciences de la Terre de Strasbourg (EOST). (1982). *GEOSCOPE, French Global Network of broad band seismic stations*. Institut de physique du globe de Paris (IPGP), Université de Paris. https://doi.org/10.18715/GEOSCOPE.G

National Oceanic and Atmospheric Administration (NOAA) (2005): Deep-Ocean Assessment and Reporting of Tsunamis (DART(R)). NOAA National Centers for Environmental Information. https://doi.org/10.7289/V5F18WNS

Scripps Institution of Oceanography. (1986). *Global Seismograph Network - IRIS/IDA* [Data set]. International Federation of Digital Seismograph Networks. https://doi.org/10.7914/SN/II

UNAVCO Community, 2004, PBO GPS Network - AB07-SandPoint_AK2004 P.S., GAGE Facility, GPS/GNSS Observations Dataset, https://doi.org/10.7283/T59W0CDH

UNAVCO Community, 2006, PBO GPS Network - AB13-ChignikLgnAK2006 P.S., GAGE Facility, GPS/GNSS Observations Dataset, https://doi.org/10.7283/T5HQ3WW8
UNAVCO Community, 2006, PBO GPS Network - AC02-AkhiokCorpAK2005 P.S., GAGE Facility, GPS/GNSS Observations Dataset, https://doi.org/10.7283/T5Z60M01
UNAVCO Community, 2008, PBO GPS Network - AC12-ChernaburaAK2008 P.S., GAGE Facility, GPS/GNSS Observations Dataset, https://doi.org/10.7283/T5NV9G7P
UNAVCO Community, 2008, PBO GPS Network - AC13-ChirikofIsAK2008 P.S., GAGE Facility, GPS/GNSS Observations Dataset, https://doi.org/10.7283/T5F18WRV
UNAVCO Community, 2005, PBO GPS Network - AC25-King_Cove_AK2005 P.S., GAGE Facility, GPS/GNSS Observations Dataset, https://doi.org/10.7283/T5SF2T4X
UNAVCO Community, 2008, PBO GPS Network - AC28-NagaiIslndAK2008 P.S., GAGE Facility, GPS/GNSS Observations Dataset, https://doi.org/10.7283/T53N21DV
UNAVCO Community, 2006, PBO GPS Network - AC34-OldHarbor_AK2006 P.S., GAGE Facility, GPS/GNSS Observations Dataset, https://doi.org/10.7283/T5028PG3
UNAVCO Community, 2005, PBO GPS Network - AC38-Quartz_CrkAK2005 P.S., GAGE Facility, GPS/GNSS Observations Dataset, https://doi.org/10.7283/T5VH5KS0
UNAVCO Community, 2007, PBO GPS Network - AC40-PortHeidenAK2007 P.S., GAGE Facility, GPS/GNSS Observations Dataset, https://doi.org/10.7283/T50G3H4S
UNAVCO Community, 2007, PBO GPS Network - AC42-SanakIslndAK2007 P.S., GAGE Facility, GPS/GNSS Observations Dataset, https://doi.org/10.7283/T5VX0DJ1
UNAVCO Community, 2006, PBO GPS Network - AC45-SitkinakIsAK2006 P.S., GAGE Facility, GPS/GNSS Observations Dataset, https://doi.org/10.7283/T5JS9NDC
UNAVCO Community, 2006, PBO GPS Network - AC67-PillarMtn_AK2006 P.S., GAGE Facility, GPS/GNSS Observations Dataset, https://doi.org/10.7283/T5Q23X61

Wessel, P., Luis, J. F., Uieda, L. A., Scharroo, R., Wobbe, F., Smith, W. H., & Tian, D. (2019). The generic mapping tools version 6. *Geochemistry, Geophysics, Geosystems*, *20*(11), 5556-5564, https://doi.org/10.1029/2019GC008515